

Chapter 5

Cross Polarization

The use of cross polarization in solid-state nuclear magnetic resonance has led to the rapid advance of experiments on spin 1/2 nuclei such as ^{13}C and ^{15}N . Both of these nuclei are very important in biological samples, especially peptides and proteins. The pioneering work with CPMAS by researchers such as Waugh and Griffin at MIT and Schaeffer at Washington University has opened the door for a variety of high resolution studies of these types of samples. A brief history of some of the theory behind cross polarization will be discussed below. Following that introduction, I will describe some of the difficulties in applying the technique of CP and CPMAS to quadrupolar nuclei and one solution to this problem.

History

The technique of cross polarization was first discovered over 30 years ago by Hartmann and Hahn.⁹² This represents one of Hahn's many contributions to the field of magnetic resonance. In these experiments, magnetic polarization is transferred from one type of nuclear spin to another. This is accomplished by applying strong rf fields along the rotating frame x axis to both types of spins following a 90° excitation pulse along the y axis. In this case, the transverse magnetizations of both spins are "spin-locked" along the rotating frame x axis. In this rotating frame, the precession rate of each spin about the spinlocking magnetization will be determined by the respective strengths of the rf fields and gyromagnetic ratios. When the Hartmann-Hahn condition is achieved, the precession frequency of both types of spins will be equal, that is to say the rf amplitude is set to a level such that the 90° pulse lengths are identical for both spin systems. Mathematically, this is expressed as $\gamma_I B_{1I} = \gamma_S B_{1S}$ for spin 1/2 nuclei. This condition is quite sharp and appears much like other resonance phenomena. The reason that this allows polarization

to be exchanged is that the flip-flop terms in the homonuclear dipolar Hamiltonian (those which mutually flip two different spins) are now zero energy processes. This greatly enhances the dipolar coupling and allows energy to be transferred between the two spin baths. The spin temperature of the two baths will rapidly come to equilibrium with the higher gyromagnetic ratio spins giving energy to the lower gyromagnetic ratio spins. This may be applied to systems such as ^1H - ^{13}C to gain approximately a factor of 3-4 in ^{13}C polarization or to ^1H - ^{15}N to gain a factor of 9-10 in ^{15}N polarization. Additionally, since the ^1H bath is high abundance, the T_1 relaxation time will often be much faster than ^{15}N or ^{13}C and the experimental repetition rate may be increased significantly⁹³. Combining cross polarization with magic-angle spinning has the added advantage of giving high resolution spectra for nuclei like carbon-13 and nitrogen-15.⁹⁴ In this respect, ^{13}C CPMAS has become a standard and routine experiment in most laboratories. In the next section, the use of cross polarization to study quadrupolar nuclei under VAS conditions will be discussed. Previously, CP has been applied to a number of different quadrupolar systems, with polarization usually being transferred from the abundant ^1H spins to the specific quadrupolar nucleus.^{28,60,65,73,95-106} I would direct the reader to these references for additional information on this subject.

Spinning Effects on CP of Quadrupolar Nuclei

Significant increases in NMR sensitivity can be achieved by transferring high nuclear spin polarization between inequivalent nuclei using cross polarization (CP) techniques. In addition, selective CP transfer can be applied as a useful tool for spectral editing. While CP is a very effective technique for static samples, the combination of CP with high-resolution solid-state NMR techniques that require sample rotation suffers from a number of difficulties. One of these difficulties is that the dipolar spin interactions that mediate the CP transfer become time dependent under magic-angle spinning (MAS) making the Hartmann-Hahn matching conditions more complicated and also reducing the

efficiency of the polarization transfer. Another difficulty arises when cross polarizing the central transition of half-integer quadrupolar nuclei. In this situation the time-dependence of the large first-order quadrupolar interaction interferes with the Hartmann-Hahn matching. Remember that even though the central transition is unaffected to first-order by the quadrupolar interaction, the energy levels themselves are affected.

Dynamic Angle Spinning (DAS) NMR was designed to provide high resolution isotropic spectra for the central transition of half-integer quadrupolar nuclei that are broadened due to second-order effects. DAS achieves this line narrowing capability by making the angle of the spinner axis a time-dependent variable. This additional degree of freedom aids not only in providing high-resolution spectra, but, as we show here provides a solution to the problem of combining cross-polarization with high-resolution solid-state NMR techniques. This solution exploits the time independence of the spin eigenvalues when spinning at 0° (parallel) to the external magnetic field direction. By performing the CP step while spinning at 0° , the full static CP intensity can be obtained and used in an MAS, variable-angle spinning (VAS), or DAS experiment.

Theory

The theory of spin locking and cross polarization of the central transition of half-odd integer nuclei has been described in detail by Vega^{96,105}. In this section, we present a condensed treatment of this problem.

In the CP experiment involving polarization transfer from a spin $I = 1/2$ to the central transition of a quadrupolar spin of $S = 3/2$, the observable of interest, $\langle S_+(t) \rangle$, is obtained from the relation

$$\langle S_+(t) \rangle = \text{Tr}\{\sigma(t)S_+\} . \quad (5.1)$$

Here $\sigma(t)$ is the density operator whose evolution is given by

$$\sigma(t) = U(t)\sigma(0)U^\dagger(t) \quad (5.2)$$

where

$$U(t) = T \exp -i \int_0^t H(s) ds , \quad (5.3)$$

T is the time ordering operator, and $H(t)$ is the Hamiltonian. The secular Hamiltonian in the rotating frame is given by

$$H(t) = H_{RF} + H_D(t) + H_Q(t), \quad (5.4)$$

where

$$H_{RF} = -\hbar\omega_{1I} I_x - \hbar\omega_{1S} S_x , \quad (5.5)$$

$$H_D(t) = \hbar\omega_D A_{20}^D(t) 2I_z S_z , \quad (5.6)$$

and

$$H_Q(t) = \hbar\omega_Q A_{20}^Q(t) \frac{1}{\sqrt{6}} \left(3S_z^2 - S(S+1) \right), \quad (5.7)$$

where ω_{1I} and ω_{1S} are the rf-field strengths for I and S spins, respectively, and $A_{20}^D(t)$ and $A_{20}^Q(t)$ are irreducible spherical tensors for the dipolar and quadrupolar interactions defined in chapter 2, respectively. It is convenient to rewrite this Hamiltonian in the fictitious spin-1/2 formalism^{26,35} (see chapter 2) as

$$\begin{aligned} H(t) = & -\hbar\omega_{1I} I_x - \sqrt{3}\hbar\omega_{1S} (S_x^{12} + S_x^{34}) - 2\hbar\omega_{1S} S_x^{23} \\ & + \sqrt{6}\hbar\omega_Q A_{20}^Q(t) (S_z^{12} - S_z^{34}) + 3\hbar\omega_D A_{20}^D(t) 2I_z S_z^{14} \\ & + \hbar\omega_D A_{20}^D(t) 2I_z S_z^{23} . \end{aligned} \quad (5.8)$$

We assume $|\omega_{1I}|, |\omega_{1S}| \gg |\omega_D|$, and transform into a time dependent frame²⁷ that diagonalizes $H_{RF} + H_Q(t)$ using

$$\begin{aligned} W(t) = & \exp -i \frac{\pi}{2} I_y \exp i \frac{\pi}{2} S_y^{14} \exp -i \frac{\pi}{2} S_y^{23} \\ & \times \exp(i2\xi_1(t)S_y^{13}) \exp(i2\xi_2(t)S_y^{24}) \end{aligned} \quad (5.9)$$

where

$$\tan 2\xi_1(t) = \frac{\sqrt{3}\omega_{1S}}{-\sqrt{6}\omega_Q A_{20}^Q(t) + \omega_{1S}}, \quad (5.10)$$

and

$$\tan 2\xi_2(t) = \frac{\sqrt{3}\omega_{1S}}{-\sqrt{6}\omega_Q A_{20}^Q(t) - \omega_{1S}}. \quad (5.11)$$

The propagator in this time dependent frame is given by

$$\tilde{U}(t) = T \exp \int_0^t \left[\tilde{H}(s) - i\hbar \dot{W}^\dagger(s) W(s) \right] ds \quad (5.12)$$

where

$$\begin{aligned} \tilde{H}(t) &= W^\dagger(t) H(t) W(t) \\ &= -\hbar\omega_{1I} I_z + \hbar\omega_{1S} (S_z^{14} - S_z^{23}) - \hbar\omega_{13}(t) S_z^{13} - \hbar\omega_{24}(t) S_z^{24} \\ &\quad - \hbar b_{IS}^{14}(t) 2I_x S_x^{14} + \hbar b_{IS}^{23}(t) 2I_x S_x^{23} - \hbar b_{IS}^{12}(t) 2I_x S_x^{12} - \hbar b_{IS}^{34}(t) 2I_x S_x^{34} \end{aligned} \quad (5.13)$$

with

$$\omega_{13}(t) = \sqrt{3\omega_{1S}^2 + \left(\sqrt{6}\omega_Q A_{20}^Q(t) - \omega_{1S} \right)^2} = \frac{-\sqrt{6}\omega_Q A_{20}^Q(t) + \omega_{1S}}{\cos 2\xi_1(t)} \quad (5.14)$$

$$\omega_{24}(t) = -\sqrt{3\omega_{1S}^2 + \left(\sqrt{6}\omega_Q A_{20}^Q(t) + \omega_{1S} \right)^2} = \frac{\sqrt{6}\omega_Q A_{20}^Q(t) + \omega_{1S}}{\cos 2\xi_2(t)} \quad (5.15)$$

$$b_{IS}^{14}(t) = \omega_D A_{20}^D(t) \{ 2\cos(\xi_1(t) - \xi_2(t)) + \cos(\xi_1(t) + \xi_2(t)) \} \quad (5.16)$$

$$b_{IS}^{12}(t) = \omega_D A_{20}^D(t) \{ 2\sin(\xi_1(t) - \xi_2(t)) - \sin(\xi_1(t) + \xi_2(t)) \} \quad (5.17)$$

$$b_{IS}^{23}(t) = \omega_D A_{20}^D(t) \{ 2\cos(\xi_1(t) - \xi_2(t)) - \cos(\xi_1(t) + \xi_2(t)) \} \quad (5.18)$$

$$b_{IS}^{34}(t) = \omega_D A_{20}^D(t) \{ 2\sin(\xi_1(t) - \xi_2(t)) + \sin(\xi_1(t) + \xi_2(t)) \} \quad (5.19)$$

and

$$i\hbar \dot{W}^\dagger(t) W(t) = 2\hbar \frac{d\xi_1(t)}{dt} S_y^{13} + 2\hbar \frac{d\xi_2(t)}{dt} S_y^{24}, \quad (5.20)$$

where $0 \leq \{\xi_1(t), \xi_2(t)\} \leq \frac{\pi}{2}$. $\tilde{U}(t)$ is related to the rotating frame propagator by $U(t) = W(t)\tilde{U}(t)W^\dagger(0)$. Equation 5.1 can be rewritten

$$\langle S_+(t) \rangle = \text{Tr}\left\{\tilde{U}(t)\tilde{\sigma}(0)\tilde{U}^\dagger(t)\tilde{S}_+\right\}, \quad (5.21)$$

where $\tilde{S}_+ = W^\dagger(t)S_+W(t)$ and $\tilde{\sigma}(0) = W^\dagger(0)\sigma(0)W(0)$. The transformed observable \tilde{S}_+ is

$$\begin{aligned} \tilde{S}_+ = & S_z^{23} \cos^2 \xi_1(t) \cos^2 \xi_2(t) + S_z^{13} \sin 2\xi_1(t) \\ & - S_z^{14} \sin^2 \xi_1(t) \sin^2 \xi_2(t) - S_z^{24} \sin 2\xi_2(t) \\ & - S_z^{12} \sin^2 \xi_1(t) \cos^2 \xi_2(t) - S_z^{34} \cos^2 \xi_1(t) \sin^2 \xi_2(t) \\ & + S_x^{13} \{ \cos \xi_1(t) \sin \xi_1(t) - \cos 2\xi_1(t) \} \\ & + S_x^{24} \{ \cos \xi_2(t) \sin \xi_2(t) + \cos 2\xi_2(t) \} \\ & + iS_y^{12} \{ \sin \xi_1(t) \cos \xi_2(t) + \cos(\xi_1(t) - \xi_2(t)) \} \\ & + iS_y^{34} \{ \cos(\xi_1(t) - \xi_2(t)) - \cos \xi_1(t) \sin \xi_2(t) \} \\ & + iS_y^{14} \{ \sin \xi_1(t) \sin \xi_2(t) - \sin(\xi_1(t) - \xi_2(t)) \} \\ & + iS_y^{23} \{ \cos \xi_1(t) \cos \xi_2(t) - \sin(\xi_1(t) - \xi_2(t)) \}. \end{aligned} \quad (5.22)$$

After an initial $\pi/2$ pulse on the I spin, the initial density operator is $\sigma(0) = I_x$, and the transformed initial density operator is

$$\tilde{\sigma}(0) = W^\dagger(0)\sigma(0)W(0) = I_z. \quad (5.23)$$

In the static case, a Hartmann-Hahn matching condition of $\omega_{1I} = (S + 1/2)\omega_{1S}$ is employed and only those spins where $|\omega_Q A_{20}^Q(\alpha, \beta, \gamma, t)| \gg |\omega_{1S}|$ (where the spatial dependence of $A_{20}^Q(t)$ is given explicitly in terms of the Euler angles of the principle axis frame) undergo polarization transfer to the central transition.

In the case of rotating samples under the above matching conditions, only those spins that satisfy $|\omega_Q A_{20}^Q(\alpha, \beta, \gamma, t)| \gg |\omega_{1S}|$ or pass through this condition during a rotor period, will undergo CP transfer, as shown by Vega. For these spins the values of $\xi_1(t)$ and $\xi_2(t)$ have values close to either 0 or $\pi/2$. When $\xi_1(t) \approx \xi_2(t) \approx 0$, $\omega_{13}(t)$ and

$\omega_{24}(t)$ are approximated by $-\omega_Q A_{20}^Q(t) + \omega_{1S}$ and $\omega_Q A_{20}^Q(t) + \omega_{1S}$ respectively, and when $\xi_1(t) \approx \xi_2(t) \approx \frac{\pi}{2}$, are approximated by $\omega_Q A_{20}^Q(t) - \omega_{1S}$ and $-\omega_Q A_{20}^Q(t) - \omega_{1S}$ respectively. In this situation, the Hamiltonian in equation 5.11 can be rewritten so that the diagonal elements are in terms of single and triple quantum transitions:

$$\begin{aligned} \tilde{H}(\xi = 0) = & -\hbar\omega_{1I} I_z - 2\hbar\omega_{1S} S_z^{23} + \sqrt{6}\hbar\omega_Q A_{20}^Q(t) (S_{00}^{14} - S_{00}^{23}) - \\ & 6\hbar\omega_D A_{20}^D(t) I_x S_x^{14} + 2\hbar\omega_D A_{20}^D(t) I_x S_x^{23} \end{aligned} \quad (5.24)$$

or

$$\begin{aligned} \tilde{H}(\xi = \frac{\pi}{2}) = & -\hbar\omega_{1I} I_z + 2\hbar\omega_{1S} S_z^{14} - \sqrt{6}\hbar\omega_Q A_{20}^Q(t) (S_{00}^{14} - S_{00}^{23}) - \\ & 2\hbar\omega_D A_{20}^D(t) I_x S_x^{14} + 6\hbar\omega_D A_{20}^D(t) I_x S_x^{23} \end{aligned} \quad (5.25)$$

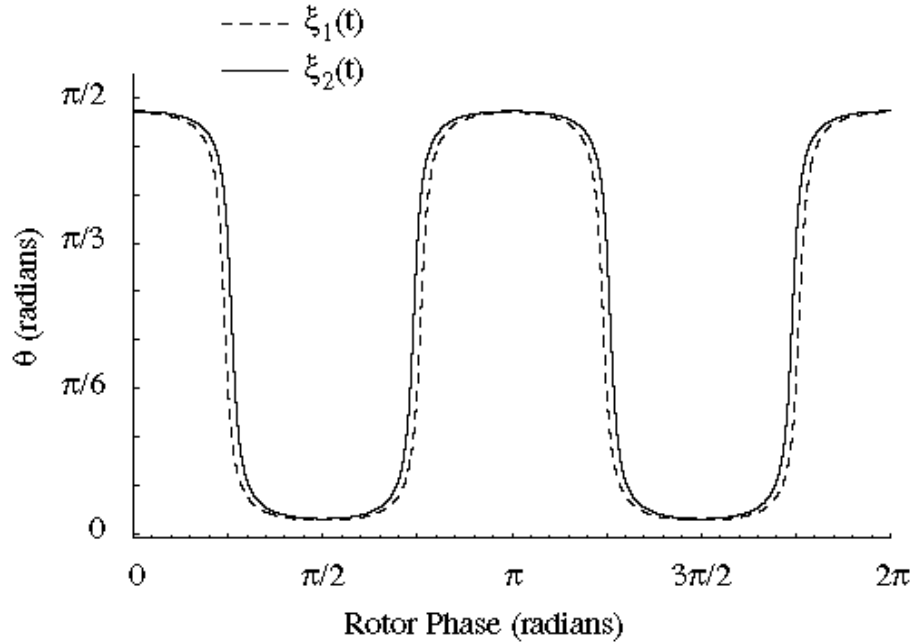


Figure 5.1 ξ_1 and ξ_2 as a Function of Rotor Phase. The values of both ξ_1 and ξ_2 stay very near their minimum (0) and maximum ($\pi/2$) values for all rotor phases, indicating that the approximations made for equation 5.24 and 5.25 are quite reasonable.

Figure 5.1 shows the graph of ξ_1 and ξ_2 as a function of rotor phase for a crystallite with a quadrupolar coupling constant of 11.0 MHz, asymmetry parameter of 0.0 whose PAS is oriented perpendicular to the rotor which is spinning about an axis oriented 54.74° from

the magic angle. Notice that the values of stay very close to the minimum and maximum values at almost all rotor phases. These curves are typical for most crystallite orientations. The Hamiltonians in equation 5.24 and 5.25 may be transformed into the RF rotating frame, assuming that $|\omega_{1I}|, |\omega_{1S}| \gg |\omega_D|$, as has been previously discussed.^{92,94}

$$\begin{aligned} I_x & I_x \cos \omega_{1I}t + I_y \sin \omega_{1I}t \\ S_x^{23} & S_x^{23} \cos 2\omega_{1S}t + S_y^{23} \sin 2\omega_{1S}t \end{aligned} \quad (5.26a)$$

$$\begin{aligned} \tilde{H}(\xi = 0) &= \hbar\omega_Q A_{20}^Q(t) (S_{00}^{14} - S_{00}^{23}) \\ &\quad - 6\hbar\omega_D A_{20}^D(t) (I_x \cos \omega_{1I}t + I_y \sin \omega_{1I}t) S_x^{14} \\ &\quad + 2\hbar\omega_D A_{20}^D(t) (I_x \cos \omega_{1I}t + I_y \sin \omega_{1I}t) \\ &\quad \times (S_x^{23} \cos 2\omega_{1S}t + S_y^{23} \sin 2\omega_{1S}t) \end{aligned} \quad (5.26b)$$

or

$$\begin{aligned} I_x & I_x \cos \omega_{1I}t + I_y \sin \omega_{1I}t \\ S_x^{14} & S_x^{14} \cos 2\omega_{1S}t - S_y^{14} \sin 2\omega_{1S}t \end{aligned} \quad (5.27a)$$

$$\begin{aligned} \tilde{H}(\xi = \frac{\pi}{2}) &= -\hbar\omega_Q A_{20}^Q(t) (S_{00}^{14} - S_{00}^{23}) \\ &\quad + 6\hbar\omega_D A_{20}^D(t) (I_x \cos \omega_{1I}t + I_y \sin \omega_{1I}t) S_x^{23} \\ &\quad - 2\hbar\omega_D A_{20}^D(t) (I_x \cos \omega_{1I}t + I_y \sin \omega_{1I}t) \\ &\quad \times (S_x^{14} \cos 2\omega_{1S}t - S_y^{14} \sin 2\omega_{1S}t) \end{aligned} \quad (5.27b)$$

Under the Hartmann-Hahn condition for the central transition, $\omega_{1I} = 2\omega_{1S}$, these equations simplify into terms which oscillate at frequencies of 0, ω_{1I} or $2\omega_{1I}$. The time dependent cosine and sine modulated terms that remain will vanish in the time average between zero crossings when $\omega_{1I} > \omega_r$, simplifying the Hamiltonians in the doubly rotating frame further.

$$\tilde{H}(\xi = 0) = \sqrt{6}\hbar\omega_Q A_{20}^Q(t) (S_{00}^{14} - S_{00}^{23}) + \hbar\omega_D A_{20}^D(t) (I_x S_x^{23} + I_y S_y^{23}) \quad (5.28)$$

or

$$\tilde{H}\left(\xi \quad \frac{\pi}{2}\right) = -\sqrt{6}\hbar\omega_Q A_{20}^Q(t) \left(S_{00}^{14} - S_{00}^{23}\right) - \hbar\omega_D A_{20}^D(t) \left(I_x S_x^{14} - I_y S_y^{14}\right) \quad (5.29)$$

Additionally, the transformed observable, \tilde{S}_+ , of Eq. [23] becomes

$$\begin{aligned} \tilde{S}_+ &= S_z^{23} \cos^2 \xi_1(t) \cos^2 \xi_2(t) - S_z^{14} \sin^2 \xi_1(t) \sin^2 \xi_2(t) \\ &+ S_x^{24} \cos 2\xi_2(t) - S_x^{13} \cos 2\xi_1(t) \\ &+ iS_y^{23} \cos \xi_1(t) \cos \xi_2(t) + iS_y^{14} \sin \xi_1(t) \sin \xi_2(t) \\ &+ iS_y^{12} \cos(\xi_1(t) - \xi_2(t)) + iS_y^{34} \cos(\xi_1(t) - \xi_2(t)) \end{aligned} \quad (5.30)$$

In general, the time-ordering operator T makes the derivation of $\tilde{U}(t)$ in Eq. [20] complicated since $\tilde{H}(t)$ and $i\hbar\dot{W}^\dagger(t)W(t)$ do not commute with themselves or each other at all times. There are however certain approximations that can simplify this task. How the system evolves depends on whether the passage through or near the zero crossing is adiabatic or sudden. In figure 5.2 the values of $\omega_{13}(t)$, $\omega_{24}(t)$, $2d\xi_1/dt$ and $2d\xi_2/dt$ are shown plotted versus $\sqrt{6}\omega_Q A_{20}^Q(t)$ for three different spinning rates (5 kHz, 1 kHz and 100Hz). It can be seen that the off diagonal $i\hbar\dot{W}^\dagger(t)W(t)$ terms are only important when the spinning is rapid and the size of the quadrupolar coupling is small. The simulation parameters are identical to those used in figure 5.1.

The adiabatic approximation is permitted when $|\tilde{H}(t)| \gg |\dot{W}^\dagger(t)W(t)|$ at all times (as in figure 5.2, 100 Hz spinning rate), and the propagator becomes

$$\tilde{U}_a(t) = \exp \left[-\frac{i}{\hbar} \int_0^t \tilde{H}(s) ds \right] \quad (5.31)$$

Under this propagator, with the Hartmann-Hahn match given above, the time dependent rotating frame initial density matrix (equation 5.24) becomes

$$\tilde{U}_a(t) \tilde{\sigma}(0) \tilde{U}_a^\dagger(t) = \tilde{U}_a(t) I_z \tilde{U}_a^\dagger(t) = \frac{1}{2} \left(I_z + S_z^{23} \right) \quad (5.32)$$

(assuming we start with a crystallite with $\xi_1(t) = \xi_2(t) = 0$) and polarization is transferred from the I -spin to the central transition of the S -spin. When the sample rotation takes the first-order quadrupolar coupling through or near zero, CP transfer from the I -

spin to the central transition of the S -spin continues, since the system is under adiabatic conditions.

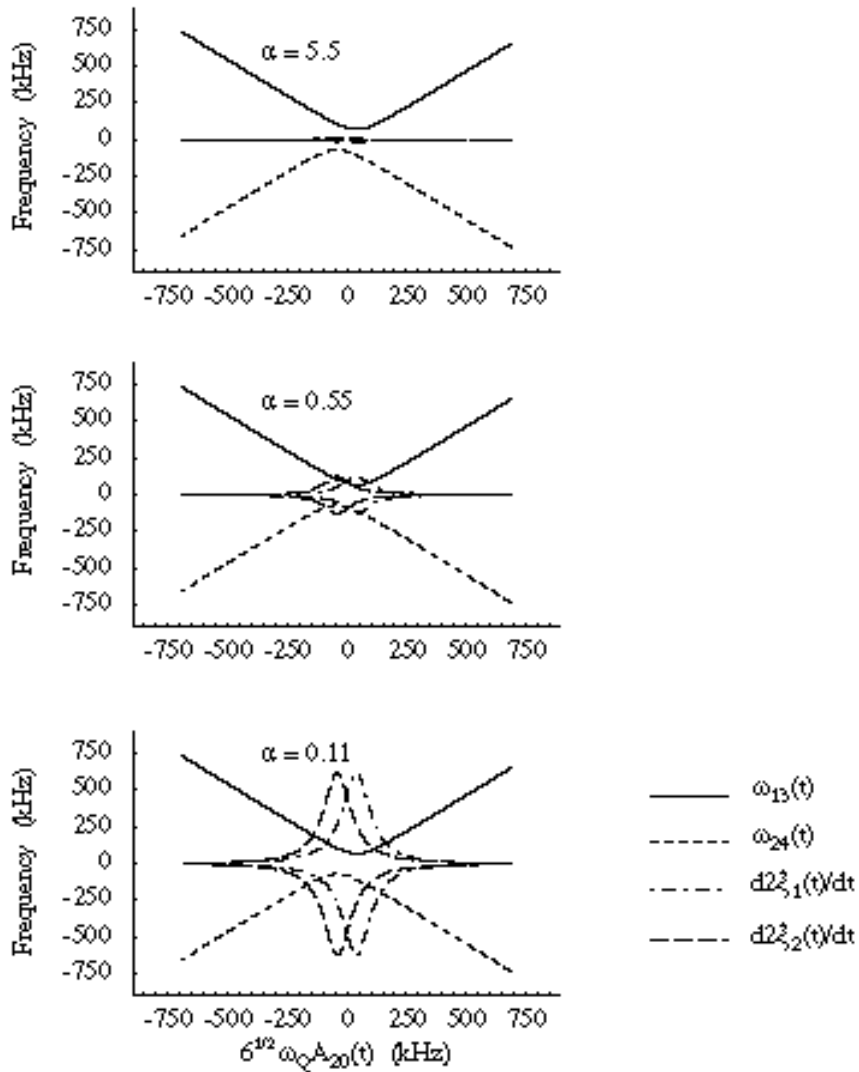


Figure 5.2 Matrix elements in cross-polarization of quadrupolar nuclei. The spinning rates are 5 kHz, 1 kHz and 100 Hz which produce adiabaticity parameters of 0.11, 0.55 and 5.5 respectively. Notice that the off-diagonal terms dominate only in the small quadrupolar coupling region and in cases of rapid spinning

Before the zero-crossing, $\xi_1(t) \approx \xi_2(t) \approx 0$ and the effective observable is therefore $\tilde{S}_+^{23} = S_z^{23} + iS_y^{23}$ (as can be seen from equation 5.23) resulting in a large observable signal. After the zero-crossing, $\xi_1(t) \approx \xi_2(t) \approx \frac{\pi}{2}$ and the effective observable is $\tilde{S}_+^{23} = -S_z^{14} + iS_y^{14}$. Therefore, the cross-polarized central-transition observable intensity $\langle S_+^{23}(t) \rangle$ goes to zero. However, since $\xi_1(t) \approx \xi_2(t) \approx \frac{\pi}{2}$, the effective adiabatic

Hamiltonian is changed to Eq. [30] and the polarization will transfer from the I -spin to the triple quantum S -spin coherence in the transformed frame. Any central coherence polarization will remain spin locked and unchanged.

$$\tilde{U}_a(t)I_z\tilde{U}_a^\dagger(t) = \frac{1}{2}(I_z + S_z^{14}) \quad (5.33)$$

This evolved coherence is exactly of the same form as our observable operator, and leads to observable intensity identical to immediately prior to the first zero crossing. After the next zero-crossing, the effective observable is transformed back into $\tilde{S}_+^{23} = S_z^{23} + iS_y^{23}$, and the central-transition begins to cross polarize again while the triple quantum coherence remains spin locked. After multiple zero-crossing cycles in the thermodynamic limit, the central and triple quantum transitions will be equally polarized from the I -spin as shown by Vega ¹⁰⁵. The state of the observable does not matter for observable intensity at this point. The overall CP intensity will be identical to that observed for a static spin in the thermodynamic limit, however the overall rate will be half as fast, since both the central and triple quantum transitions are being polarized simultaneously. In the presence of a short rotating frame relaxation time, this will lead to a reduced overall CP intensity from adiabatic spins.

The sudden approximation is permitted when (as in figure 5.2, 5 kHz spinning speed) at the zero-crossing, $|\tilde{H}(t)| \ll |\dot{W}^\dagger(t)W(t)|$. The propagator is then

$$\tilde{U}_s(t) = \exp \int_0^t \dot{W}^\dagger(s)W(s)ds \quad (5.34)$$

This propagator transforms the S_z^{23} and S_z^{14} in the following manner:

$$\tilde{U}_s(t)S_z^{23}\tilde{U}_s^\dagger(t) = S_z^{14} \quad (5.35)$$

$$\tilde{U}_s(t)S_z^{14}\tilde{U}_s^\dagger(t) = S_z^{23} \quad (5.36)$$

The transformed initial density operator before the first zero-crossing is still given by equation 5.32. However, during the first zero-crossing, the S_z^{23} term is transformed to S_z^{14} .

In the sudden reversal of the first-order quadrupolar coupling, the cross-polarized central-transition is transferred to the triple quantum transition after the reversal. The observable intensity after the zero-crossing is therefore identical to that immediately before the zero-crossing. After the first zero-crossing, the CP transfer from the I -spins to the triple quantum coherence will continue according to equation 5.33. Therefore the observable operator will always match the cross polarizing transition. After multiple zero crossings, one of the two transitions will be completely polarized while the other will be unpolarized. The polarized intensity will always remain observable and the CP efficiency and rate should be identical to the static case.

For crystallites which pass through the zero crossing in neither an adiabatic or sudden regime fall into the intermediate regime (see figure 5.2, 1 kHz spinning speed). This type of evolution is the most difficult of the three cases to calculate. To determine the evolution of the density matrix in the intermediate regime, we need to include both the diagonal $\tilde{H}(t)$ and the off diagonal $\dot{W}^\dagger(t)W(t)$ contributions to the unitary evolution propagator. These two terms do not commute with each other and the time ordering operator may not be easily removed. The solution to this problem is to rediagonalize the net Hamiltonian at each time step. There does not appear to be an easy method for doing this diagonalization. Vega has shown with numerical simulations that spins undergoing an intermediate regime zero crossing evolve into non-spin locked states^{96,105}. Therefore, the contribution these spins make will only be prior to their first zero-crossing, after which their contribution to the overall observed cross polarization intensity will decay rapidly.

We have performed variable spinning angle cross-polarization experiments which may be approximately described with the above results. For a powdered sample, we may classify each spin according to its PAS orientation with respect to the rotor in one of five categories. These categories are:

1. Spins with large $\omega_Q A_{20}^Q(t)$ which undergo no zero crossings (essentially static spins, alternatively spins which have ξ_1 and ξ_2 approximately equal to either 0 or $\pi/2$ for all time),
2. Spins which have a small $\omega_Q A_{20}^Q(t)$ for the majority of a rotor period (alternatively those spins which only have small oscillations in ξ_1 and ξ_2 about $\pi/4$),
3. Spins which have a large $\omega_Q A_{20}^Q(t)$ for most of the rotor period and undergo adiabatic regime zero crossings (alternatively those spins for which ξ_1 and ξ_2 oscillate between 0 and $\pi/2$),
4. Spins which have a large $\omega_Q A_{20}^Q(t)$ for most of the rotor period (just as in 3) and undergo sudden regime zero crossings,
5. Spins which have a large $\omega_Q A_{20}^Q(t)$ for most of the rotor period (just as in 3 and 4) and undergo intermediate regime zero crossings.

For spins which fall into the first and fourth categories, the cross polarization contributions are simple, as they will contribute full intensity with normal polarization build up rates. For the spins in the fifth category, the cross polarization contribution is also simple to calculate, since in the limit of long contact times, they will contribute no cross polarization intensity. For spins in the second category, the Hartmann-Hahn match condition will not be met for a significant portion of the total contact time and the contribution will again go to zero to the overall cross polarization intensity. For spins in the third category, the cross polarization contribution will be identical to the static or sudden spins, however the build up rate will be half as fast.

The only difficulty remaining is to determine mathematically the definition for each of these five categories. The first category is the most easy to define, as this constitutes spins for which $|\sqrt{6}\omega_Q A_{20}^Q(t)| > 5\omega_{15}$ at all times (corresponding to ξ_1 and ξ_2 within $\pi/12$ of the minima and maxima of 0 or $\pi/2$). The extent to which the quadrupolar coupling must be larger than the radio frequency strength is difficult to define exactly, but

generally a factor of five or more is probably sufficient to fully truncate the radio frequency portion of the Hamiltonian. The second category is likewise simple in definition, as this represents the spins for which $|\sqrt{6}\omega_Q A_{20}^Q(t)| > 5\omega_{1S}$ for more than one third of a rotor period. The factor of one third is an arbitrary number which seems to work well in practice. This in general will represent only the spins whose PAS z-axis lies near the magic-angle under sample rotation. The third, fourth and fifth categories relate to spins which spend a majority of their time (more than two-thirds of a rotor period) with $|\sqrt{6}\omega_Q A_{20}^Q(t)| > 5\omega_{1S}$. To differentiate between these three cases, the ratio of the sizes of $|\tilde{H}(t)|$ and $|\dot{W}^\dagger(t)W(t)|$ at the zero crossing must be considered. This leads to the definition of an adiabaticity parameter α below.

$$\begin{aligned}
|\tilde{H}(t)| &= \sqrt{3\omega_{1S}^2 + \left(\sqrt{6}\omega_Q A_{20}^Q(t) - \omega_{1S}\right)^2} \\
|\dot{W}^\dagger(t)W(t)| &= 2 \frac{d\xi_1(t)}{dt} = \frac{\sqrt{18}\omega_{1S}\omega_Q}{3\omega_{1S}^2 + \left(\sqrt{6}\omega_Q A_{20}^Q(t) - \omega_{1S}\right)^2} \frac{dA_{20}^Q(t)}{dt} \\
\alpha &= \frac{3\omega_{1S}^2 + \left(\sqrt{6}\omega_Q A_{20}^Q(t_0) - \omega_{1S}\right)^2}{\sqrt{18}\omega_{1S}\omega_Q \left. \frac{dA_{20}^Q(t)}{dt} \right|_{t_0}}
\end{aligned} \tag{5.37}$$

This is then evaluated at the zero crossing where $\sqrt{6}\omega_Q A_{20}^Q(t_0) = \omega_{1S}$. At this point the value of ξ_1 goes through $\pi/4$ and the adiabaticity parameter is then

$$\alpha = \frac{3\omega_{1S}^2}{\sqrt{6}\omega_Q \left. \frac{dA_{20}^Q(t)}{dt} \right|_{t_0}} \tag{5.38}$$

Alternatively one could define an adiabaticity factor based on ω_{24} and $2d\xi_2/dt$, however this gives an identical result at the $2d\xi_2/dt$ resonance where $\sqrt{6}\omega_Q A_{20}^Q(t_0) = -\omega_{1S}$. Explicitly evaluating this derivative yields

$$\begin{aligned}
A_{20}^Q(t) &= \sum_{m=-2}^2 \sum_{n=-2}^2 e^{-i(m\omega_r t + n\alpha + m\gamma)} d_{m0}^{(2)}(\theta) d_{nm}^{(2)}(\beta) \rho_{2n} \\
\frac{dA_{20}^Q(t)}{dt} &= \omega_r \sum_{m=-2}^2 \sum_{n=-2}^2 -ime^{-i(m\omega_r t + n\alpha + m\gamma)} d_{m0}^{(2)}(\theta) d_{nm}^{(2)}(\beta) \rho_{2n} \\
&= \omega_r B_{20}^Q(t) \\
\alpha &= \frac{3\omega_{1s}^2}{\omega_Q \omega_r B_{20}^Q(t_0)}
\end{aligned} \tag{5.39}$$

This definition of adiabaticity parameter is proportional to the one used by Vega in his description of cross polarization¹⁰⁵, however, now there is an additional orientation dependence as well which comes from the time derivative of $A_{20}^Q(t)$. When the value of α is much larger than one, then the diagonal terms dominate in the evolution and the spin will be categorized in group three (adiabatic). When the value of α is much less than one, then the off-diagonal terms dominate at the zero crossing and the spin will be categorized in group four (sudden). When α is of the order of one, then the spins are classified as group five (intermediate). To calculate the approximate cross polarization efficiency at a given spinning angle, we merely calculate the number of spins in each category and add the cross polarization intensity proportionally for each category. The adiabatic contribution is the most difficult to estimate as the build up rate is half as fast and therefore may not be fully cross polarized before rotating frame relaxation begins to impede the buildup. In any case the adiabatic contribution should lie somewhere between the 50% and 100% intensity contribution levels.

The theory for the dynamic-angle spinning experiment has been described previously in chapter 3. Remember that in the DAS experiment, there exists a continuous distribution of angle pairs which lead to high resolution isotropic spectra. Specifically, the $k = 1$ and $k = 5$ angle pairs will be evaluated under CP conditions. I have done experiments which compare CP efficiency at a variety of spinning angles.

Experiments on Sodium Pyruvate and Sodium Hydroxide

The cross polarization experiments were performed on a home built spectrometer based on a Techmag acquisition system at 7.04 T (^1H NMR frequency of 301.200 MHz and ^{23}Na frequency of 79.671 MHz).

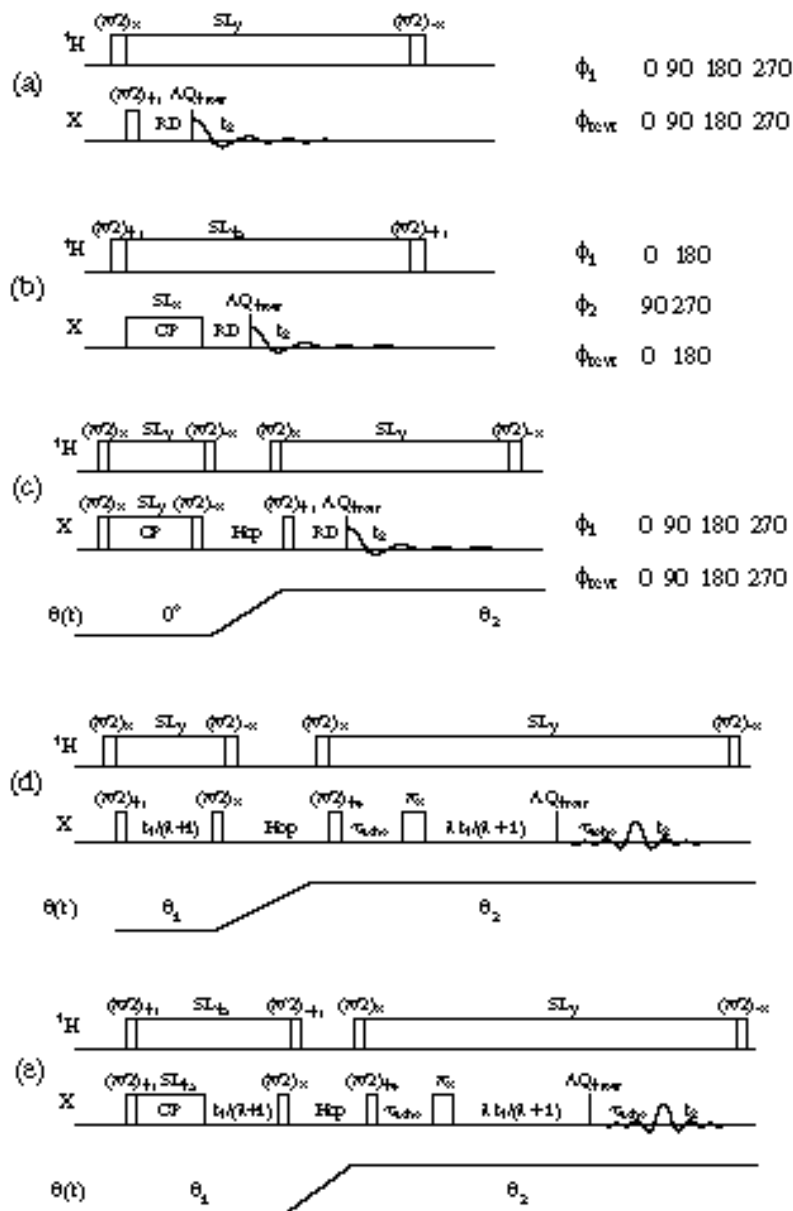


Figure 5.3 Cross-Polarization Pulse Sequences. Phase cycles are indicated for the one dimensional experiments (a-c) which are one pulse with decoupling, cross polarized with decoupling and zero-polarized with decoupling and sample spinning axis reorientation. The (d-e) pulse sequences are the normal and CP two dimensional DAS experiments respectively. The phase of the 90° pulses on X are identical to those in the SEDAS experiment. The spin lock pulse is always set to the phase of the first pulse plus 90° .

The DAS probe was home built with a stationary 0.75" diameter coil for both rf-transmission and detection as described by Mueller *et al.*⁵¹ The double-tuned resonant circuit was similar to one described by Doty *et al.*¹⁰⁷ The spinning rate was between 4.0 and 6.6 kHz. The samples of sodium hydroxide, NaOH·xH₂O, and sodium pyruvate, CH₃OCOONa, used for these experiments were obtained from standard commercial sources. The pulse programs and phase cycles are given in figure 5.3 below. The DAS pulse sequence has been described previously in chapter 4. For the CP efficiency experiments, phase alternation of the ¹H rf was used (figure 5.3b) to assure that only the intensity due to CP would be measured. For CPDAS and ZPVAS experiments (figure 5.3a and 5.3c), a 90° pulse was applied on ²³Na simultaneously with the initial ¹H 90° to achieve the largest final sodium polarization. For the ²³Na spectra without CP, recycle delays of 30s and 16 s were used for NaOH and CH₃OCOONa, respectively, while, for the CP experiments, recycle delays of 10 minutes and 36 s were used, respectively. For the DAS experiments, we acquired 32 scans plus 1 dummy scan for each of the 90 *t*₁ points while for the CP build up curves and ZPVAS spectra we acquired either 4, 8, or 64 scans plus 2 dummy scans for each different contact time and angle pair respectively. For the CPDAS and ZPVAS experiments on CH₃OCOONa the CP contact time was 20 ms. The contact time for NaOH 2 ms. The input power of 200W on the ¹H channel and 100W on the ²³Na channel gave 7 μs central transition selective 90° pulses. The CP Hartmann-Hahn match condition was achieved by setting $\gamma_H B_{1,H} = (I + 1/2) \gamma_{Na} B_{1,2} = 2 \gamma_{Na} B_{1,Na}$ which will selectively polarize the central (1/2 -1/2) transition since the central transition nutation frequency is $\omega_{nutation} = (S + 1/2) \gamma_{Na} B_{1,Na}$ in the presence of a large quadrupolar interaction^{6,27,28,35}. Methods of simulating powder patterns have been described previously in chapter 2 and in additional papers^{41,76,81}.

Cross Polarization Results and Discussion

The effect of level crossings on CP efficiency can be seen clearly below in figure 5.4, which shows the cross polarization efficiencies of NaOH and sodium pyruvate versus VAS spinning angle. All intensities are scaled relative to the corresponding single pulse ^{23}Na VAS and MAS spectra, using the sequence in figure 5.3a.

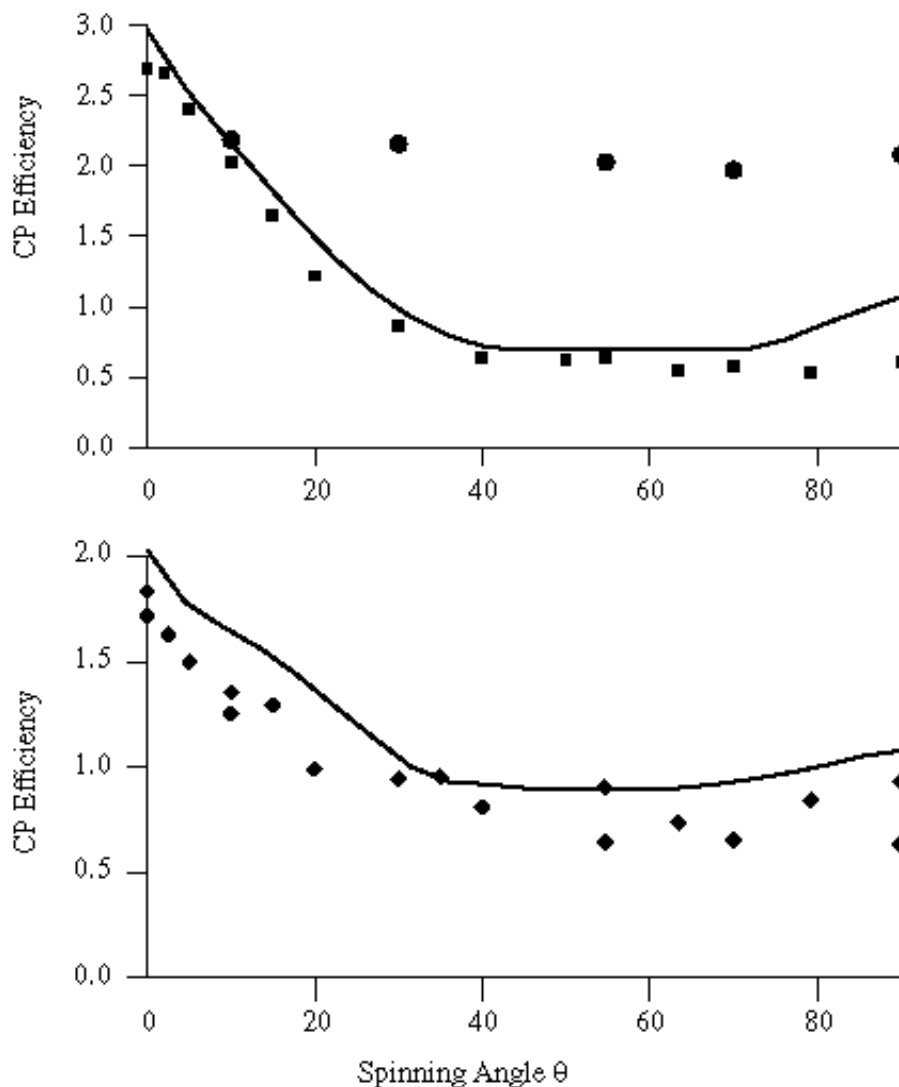


Figure 5.4 CP Efficiency versus Spinning Angle. The upper graph shows the cross polarization efficiency (boxes) for sodium pyruvate. The circles in this graph indicate the effective polarization under ZPVAS (rather than CPVAS). The line indicates the theoretical curve from the model described in the previous section. The lower graph shows the CP efficiency (diamonds) for sodium hydroxide. The line again represents the approximate theoretical efficiency.

As expected, only under static (0° VAS) conditions do we achieve the expected CP efficiency maximum of approximately $\gamma_1/2\gamma_2 = 1.9$ for sodium hydroxide (NaOH) and $3\gamma_1/4\gamma_2 = 2.84$ for sodium pyruvate ($\text{CH}_3\text{OCOO}^- \text{Na}^+$). The factor of 1/2 and 3/4 are due to the high abundance (basically 100%) of both the ^1H and ^{23}Na isotopes causing cross polarization to be controlled by the equilibrium between their respective spin temperatures and heat capacities (related to the number of protons and sodium atoms per molecule). As the VAS angle increases, CP efficiency decreases dramatically. As seen in figure 5.4, spinning the sample at an angle greater than approximately 30° results in a CP efficiency that is less than that achieved by a single pulse. This indicates that the level crossings are significant, even when only a reduced fraction of the spins are undergoing the maximum four crossings per rotor cycle. For DAS purposes, the only angle pairs which will have an angle less than 30° will be those with high k values. This immediately points to the $k = 5$ experiment, since this has added advantages of fastest effective spinning rate and narrowest homonuclear dipolar linewidths (see chapter 3).

The dashed theoretical fits in figure 5.4 were obtained by numerically calculating the curves according to the theory outlined in the previous section. For NaOH and CH_3OCOONa , the values of e^2qQ/h were 1.8 and 2.36 MHz and η_Q were 0.0 and 0.77 respectively. The parameters for sodium pyruvate were obtained from simulations of the MAS spectrum while those of sodium hydroxide were taken from Vega.¹⁰⁵ Qualitatively, the theoretical CP efficiency curves are approximately what one would expect, with the greatest CP enhancement for VAS angles near 0° .

Figure 5.4 also shows CP efficiency for sodium pyruvate at the angle at which detection occurred under ZPVAS. Since CP always occurs at 0° , the observed efficiency is constant for all angles. However, the efficiency under ZPVAS is less than that observed under 0° CPVAS because of T_1 relaxation processes that occur during the hop from 0° to the detection angle.

In figure 5.5 we show the ^1H decoupled MAS spectra of sodium pyruvate acquired with and without CP and with ZPMAS along with the simulation of the MAS powder pattern. The signal-to-noise is the worst for CPMAS—about 75% of that seen in the MAS spectrum without CP.

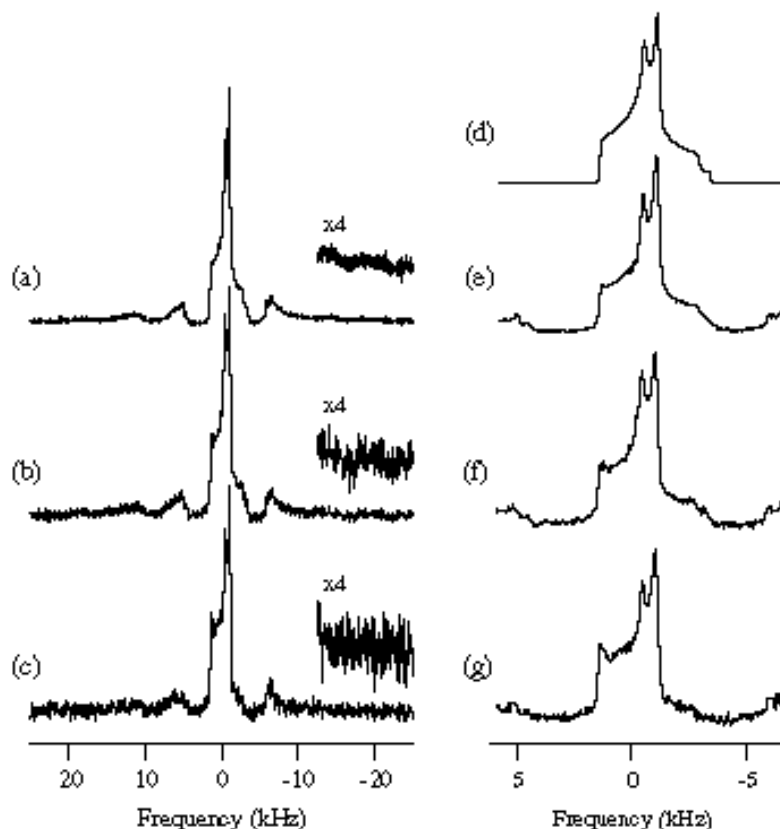


Figure 5.5 Comparison of CPMAS, MAS and ZPMAS Experiments. (a) and (e) show ZPMAS spectra, (b) and (f) show 1-pulse MAS spectra, (c) and (g) show CPMAS spectra and (d) shows the high speed MAS simulation.

On the other hand, the ZPMAS spectrum has a signal-to-noise ratio about twice that seen in the MAS spectrum taken without CP. This is expected since very little of the static cross polarized magnetization should decay by T_1 processes during the hop from 0° to 54.74° while the cross polarization efficiency under MAS is so poor.

In figure 5.6, the decoupled DAS and CPDAS spectra of sodium pyruvate for the 0° - 63.43° ($k = 5$) and 37.38° - 79.19° ($k = 1$) angle pairs are compared. As can be seen in figure 5.4, for $k = 5$, we observe over 2.5 times the signal-to-noise in the spectrum taken

with CP compared to the spectrum taken without CP. In addition, the CPDAS experiment at $k = 5$ has a S/N ratio over 4.5 times that of the CPDAS experiment at $k = 1$. This demonstrates the importance of 0° cross polarization for DAS. The CPDAS experiment done at 37.38° ($k = 1$) has a worse S/N than the same experiment done

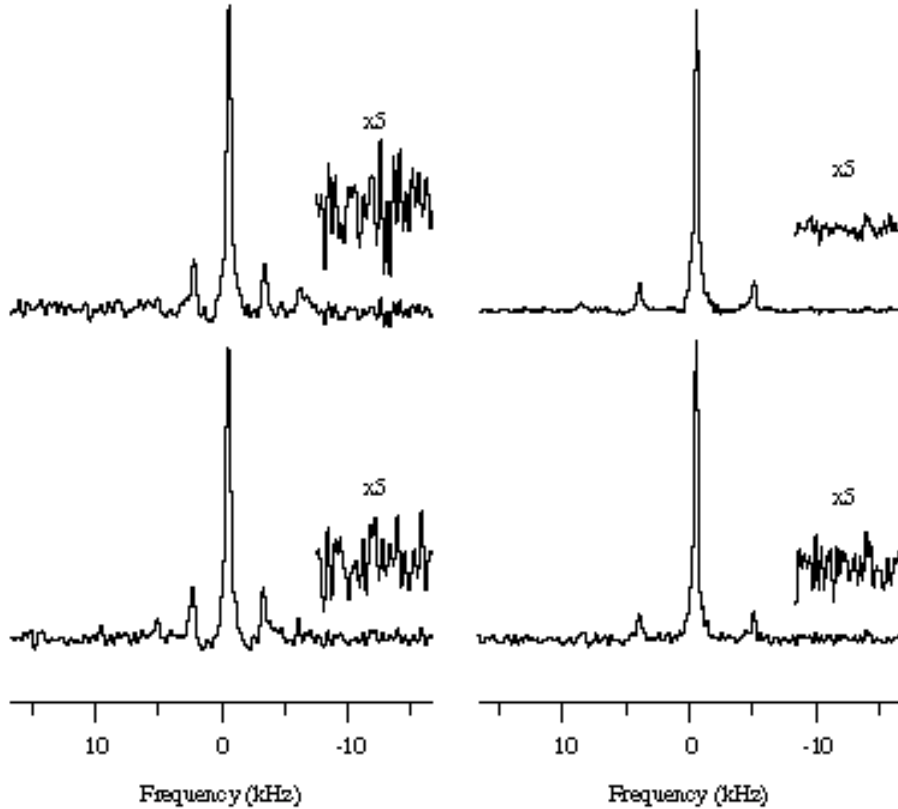


Figure 5.6 Comparison of CPDAS (fig 5.3e) versus DAS (fig 5.3d). The spectra on the right are $k=5$ DAS spectra while the spectra on the left are $k=1$. The upper spectra in both cases are from CPDAS.

without cross polarization. In fact, the CP efficiency under CPDAS at $k=1$ is very similar to that observed under VAS at 37.38° (figure 5.2), which is to be expected. Other k values will also have reduced CP efficiencies, in addition to having spinning sideband patterns which are more complicated than in the $k = 1$ or 5 cases (see chapter 3). In table 5.1, the absolute signal-to-noise ratios for each the experiments in figure 5.6 are presented.

We have shown that the efficiency of CP is influenced very little by the choice of spinning angle until the angle approaches 0° . Therefore, in any VAS or DAS experiment

it will be difficult to achieve maximum CP efficiency unless one does the magnetization transfer at 0° as a part of, or before starting the experiment.

Experiment	Angle Pair	Signal to Noise Ratio
CPDAS (fig 5.3e)	k=5 (0.00° , 63.43°)	123.6
CPDAS (fig 5.3e)	k=1 (37.38° , 79.19°)	27.3
Normal DAS (fig 5.3d)	k=5	49.1
Normal DAS (fig 5.3d)	k=1	32.3

Table 5.1 Signal to Noise Ratios in CPDAS and Normal DAS

In addition, for the case of DAS the choice of 0° and 63.43° possesses the additional benefit of giving the largest effective spinning speed, $5\omega_r/6$, and narrowest residual homonuclear dipolar linewidth (see chapter 3). These results should prove quite valuable for systems with low abundance such as ^{87}Rb (27.8% abundant) or where isotopic labeling is crucial ^{17}O (0.037% abundant) which could have polarization enhancements of 3.1 and 7.4 respectively leading to large savings in experiment time. In addition, for spin 1/2 systems (such as ^1H - ^{13}C or ^1H - ^{15}N), where the time modulation of the dipolar interaction leads to modulations of the Hartmann-Hahn match condition, the use of ZPMAS may yield better CP efficiencies and reduced CPMAS distortions.